

Multilevel cloud structures over Svalbard

Andreas Dörnbrack¹ and Sonja Gisinger

Institut für Physik der Atmosphäre, DLR Oberpfaffenhofen, Germany

Michael C. Pitts

NASA Langley Research Center, Hampton, Virginia 23681 USA

Lamont R. Poole

Science Systems and Applications, Incorporated, Hampton, Virginia 23666 USA

Marion Maturilli

Alfred Wegener Institute, Helmholtz Centre for Polar and Marine Research,

Telegrafenberg A43, D-14473 Potsdam

¹ Corresponding author: Andreas Dörnbrack, DLR Oberpfaffenhofen, Institut für Physik der Atmosphäre,

Münchener Str. 20, D – 82234 Wessling, Germany, Email: andreas.doernbrack@dlr.de

24 **Abstract**

25

26 The presented picture of the month is a superposition of space-borne lidar observations and high-
27 resolution temperature fields of the ECMWF integrated forecast system (IFS). It displays
28 complex tropospheric and stratospheric clouds in the Arctic winter 2015/16. Near the end of
29 December 2015, the unusual northeastward propagation of warm and humid subtropical air
30 masses as far north as 80°N lifted the tropopause by more than 3 km in 24 h and cooled the
31 stratosphere on a large scale. A widespread formation of thick cirrus clouds near the tropopause
32 and of synoptic-scale polar stratospheric clouds (PSCs) occurred as the temperature dropped
33 below the thresholds for the existence of cloud particles. Additionally, mountain waves were
34 excited by the strong flow at the western edge of the ridge across Svalbard, leading to the
35 formation of mesoscale ice PSCs. The most recent IFS cycle using a horizontal resolution of 8
36 km globally reproduces the large-scale and mesoscale flow features and leads to a remarkable
37 agreement with the wave structure revealed by the space-borne observations.

38 **1 Introduction**

39 The “picture of the month” as presented in this short contribution is not a photo of the sky
40 spontaneously shot from a digital camera. The picture as displayed in Figure 1 is a combination
41 of space-borne measurements by the CALIOP (Cloud-Aerosol Lidar with Orthogonal
42 Polarization) instrument onboard the CALIPSO (Cloud-Aerosol Lidar and Infrared Pathfinder
43 Satellite Observations) satellite during one of several Arctic overpasses on 30 December 2015
44 and a high-resolution short-term forecast of a numerical weather prediction (NWP) model
45 utilizing an unprecedented global resolution of about 8 km (for data sources, see Appendix). In
46 our days of ceaseless swells of pictures taken everywhere and anytime on the planet, a snapshot
47 taken from a sensor much different than a camera, taken from a perspective so much different
48 than from Earth, and superimposed with numerical predictions reflecting the observed flow
49 features with a remarkable realism elicits wonder and admiration.

50 The selected “picture of the month” displays tropospheric and stratospheric cloud structures
51 which appeared simultaneously during a remarkable meteorological situation in the high Arctic
52 near Svalbard on 30 December 2015. The resulting spectacular and uncommon appearance of
53 diverse cloud types and structures at different layers reaching up to 28 km altitude was
54 documented by the CALIOP measurements of total attenuated backscatter at 532 nm (Fig. 1a).
55 The CALIOP observations show an extensive, elongated structure of cirrus clouds within the
56 upper troposphere up to an altitude of about 13 km. The cirrus clouds are also nicely seen in the
57 infrared satellite image at this time (Fig. 2). Slightly more than 6 km above this cirrus deck,
58 CALIOP detected a nearly 8 km deep layer of synoptic-scale polar stratospheric clouds (PSCs)
59 embedded in an extended cold layer with temperatures less than 191 K. Within this layer,
60 vertically tilted and horizontally separated patterns of enhanced attenuated backscatter are
61 collocated with cold stratospheric temperature values less than 185 K (Fig. 1b). They are

62 reminiscent of mountain-wave induced PSCs (e.g. Maturilli and Dörnbrack, 2006, Fig. 9). This
63 first, qualitative interpretation is supported by the very structured PSCs occurring in a region both
64 above and downstream of Svalbard's mountains and above the underlying clouds near the
65 tropopause as mentioned above. As shown later, the satellite trace as sketched in Figs, 3 and 6
66 was nearly parallel to the stratospheric winds and the mountain-wave induced temperature are
67 tilted into the ambient wind.

68 The spectacular display of PSCs¹ has fascinated people for a long time and they have been
69 observed scientifically since the 1880s (e.g. Backhouse, 1885, Geelmuyden, 1885, Mohn, 1893,
70 Stanford and Davies, 1974). A first step to explain the nature of these clouds was the exact
71 determination of their height range between 20 and 30 km by Störmer (1929, 1931). During the
72 recent thirty years, PSCs were systematically monitored because chemical reactions on cloud
73 particles play a major part in the depletion of the ozone layer (Solomon, 1999). The reactions are
74 very efficient at low temperatures due to the increase in particle surface area and in
75 heterogeneous reaction rates (Peter, 1997). The large interannual variability of the Arctic polar
76 vortex and of the polar cap minimum temperatures attained during northern hemispheric winters
77 (Fig. 3) regularly sparks off the scientific interest about the possible formation of PSCs and the
78 consequential ozone depletion in spring. For an overview of the evolution of the recent winter
79 2015/2016, see the excellent overview by Manney and Lawrence (2016).

80 PSCs form in a variety of ways. First of all, the ambient stratospheric temperatures must
81 fall below a certain threshold where liquid or solid particles can form. Here, different freezing
82 processes (homogeneous and/or heterogeneous freezing) determine the composition of the PSC
83 particles. Generally, one differentiates between ice PSCs, which can exist at $T < T_{\text{FROST}}$, solid
84 nitric acid trihydrate (NAT) PSCs, which can exist at $T < T_{\text{NAT}} (\approx T_{\text{FROST}} + 7 \text{ K})$, and liquid

¹ These clouds are often called mother-of-pearl clouds because of their magnificent display of spectral colors.

85 supercooled ternary solution (STS; $\text{HNO}_3/\text{H}_2\text{O}/\text{H}_2\text{SO}_4$) PSCs, which can exist at $T \lesssim T_{\text{FROST}} + 3$
86 K. Since T_{FROST} depends on atmospheric humidity it varies with altitude ($T_{\text{FROST}} \approx 188$ K at 50
87 hPa and $T_{\text{FROST}} \approx 185$ K at 30 hPa). PSCs can be observed in-situ by instruments flying on
88 balloons (e.g. Rosen et al., 1992) or by in-situ airborne sensors (e.g. Dye et al., 1996). The high
89 altitudes and vertical extent of PSCs favor remote-sensing systems such as lidars operated on
90 ground (e.g. di Liberto et al., 2014), on aircraft (e.g. Browell et al., 1990), or on satellites (e.g.
91 Strawa et al., 2002). Most of the recent studies on PSCs focused on the composition and sizes of
92 the particles (e.g. Reichardt et al., 2015) and chemical processes occurring at their surfaces that
93 yield ozone-destructive, reactive chlorine species (e.g. Solomon, 1999).

94 Numerical modelling of PSCs has always been a challenging task as chemical and
95 dynamical aspects of their formation and existence must be combined (e.g., Reichardt et al.,
96 2004). Their formation is primarily influenced by large-scale processes such as the radiative
97 cooling inside the Arctic polar vortex. Moreover, it is known that both synoptic-scale as well as
98 mesoscale weather systems influence the formation of PSCs and the associated chemical
99 reactions (Teitelbaum and Sadourny, 1998, Carslaw et al., 1998). Simulation of mesoscale
100 mountain waves especially posed a challenge, and special methods such as linear wave prediction
101 models and mesoscale forecast models were used in the past to predict their local formation (e.g.,
102 Dörnbrack et al., 1998, Eckermann et al., 2006). In this day and age, global operational NWP
103 models use spatial resolutions which hardly could be attained by limited area models several
104 years ago. For example, the European Centre of Medium-Range Weather Forecasts (ECMWF)
105 currently runs its operational predictions of the Integrated Forecast System (IFS) cycle 41r2 at 8
106 km globally (Hólm, et al, 2016, Malardel and Wedi, 2016). Here, it will be shown that the
107 conditions under which the observed mesoscale ice PSCs formed can be resolved by the IFS..

108

109 **2. Weather Situation and Gravity Wave Characteristics**

110 *Cold Arctic Polar Vortex*

111 The composite “picture of the month” was taken in a period when the temperatures inside
112 the Arctic stratospheric vortex were unusually cold (Fig. 3). In November/December 2015, the
113 Arctic vortex was minimally disturbed by upward propagating planetary waves and the polar cap
114 minimum temperature T_{MIN} between 65°N and 90°N dropped well below the climatological
115 mean. The red T_{MIN} -line in Fig. 3 reveals that the threshold of T_{NAT} at 50 hPa was already
116 reached at the beginning of December 2015, and T_{MIN} dropped below T_{FROST} at the end of 2015.
117 Apparently, the minimum temperatures falling below T_{FROST} at the end of the year constitute a
118 new record. In its further evolution, the Arctic polar vortex remained cold, stable and coherent
119 until end of February 2016 (Manney and Lawrence, 2016). The final warming already occurred
120 early at the beginning of March 2016 in accordance with the findings of the climatological study
121 of Hu et al. (2014). In such a cold stratospheric environment, the period of temperatures below
122 T_{FROST} and T_{NAT} at 50 hPa lasted more than one month and three months, respectively. CALIPSO
123 observations until the end of January 2016 confirm the widespread occurrence of PSCs in the
124 Arctic.

125 *Tropospheric Flow Conditions*

126 Near the end of December 2015, the tropospheric flow over the Northern Atlantic was
127 characterized by an anticyclonic Rossby wave breaking event. Figure 4 illustrates the late stages
128 of this event by means of the height and wind at the 2 PVU surface from the ECMWF operational
129 analyses valid on 29 December 2015 at 18 UTC and twelve hours later on 30 December 2015 at
130 06 UTC, respectively. A ridge with tropopause heights of up to 13 km extended north to latitudes

131 above 80°N. Between this ridge with high surface pressure (maximum at about 1038 hPa) over
132 Eastern Europe and a surface pressure low over Greenland (minimum at about 968 hPa), a strong
133 south-westerly low-level flow extended over the entire northern Atlantic and the Norwegian Sea
134 towards Svalbard (Fig. 5 a, b). East of Greenland, warm and moist air was advected northwards
135 as shown by the increased values of the equivalent potential temperature (Fig. 5 c, d). Further
136 south near Iceland, a storm with a core pressure of 930 hPa on 30 December 2015 at 06 UTC
137 propagated north. This weather situation led to a combination of two processes relevant for the
138 cloud structures as shown in Fig. 1. First, the increase of the tropopause height associated with
139 the anticyclonic Rossby wave breaking led to a cooling of the air masses in the upper troposphere
140 and lower stratosphere (UTLS) due to adiabatic expansion. Secondly, the strong troposphere-
141 deep pressure gradient between the upstream Greenland/Iceland cyclone complex and the
142 downstream Scandinavian ridge forced a strong flow across the mountains of Svalbard which
143 reached a maximum at 30 December 2015 at 00 UTC with horizontal winds larger 25 m s^{-1} at 700
144 hPa (Fig. 5 e, f).

145 A series of five radiosonde ascents from Ny-Ålesund, Svalbard covering the period from 27
146 to 31 December 2015 (Fig. 6) illustrates the previous findings from the IFS analyses. First of all,
147 the warming of the troposphere by about 15 K due to the warm-air advection can be clearly seen
148 in Fig. 6a. During the same period, the tropopause rose and sharpened dramatically. Indeed, the
149 vertical temperature profiles of 29 and 30 December 2015 at 12 UTC are more typical for a mid-
150 latitude station than for an Arctic location.

151 *Large-scale cooling*

152 An analysis of radiosonde soundings from Ny-Ålesund, Svalbard (79°N, 12°E) reveals a
153 drop of the mean temperature between 10 and 13 km by about 9 K in three days reaching 200 K

154 on 29 December (see Table 1). This strong cooling associated with the tropopause ascent led to
155 the formation of the observed cirrus clouds at these levels. Not only the temperature in the
156 vicinity of the tropopause dropped, but the mean stratospheric temperature between 20 and 25 km
157 altitude also decreased by about 4 K due to the lifting of the atmosphere above the ridge (Table
158 1). In this way, the mean temperatures near 30 hPa dropped below 185 K, the ice existence
159 temperature T_{FROST} . However, increased backscatter values indicative of ice PSCs appear
160 primarily at and leeward of the wave crests as shown in Figure 1a. The adiabatic cooling by
161 ascending air parcels leads to a local temperature decrease and to ice nucleation which require
162 temperatures $T \lesssim T_{\text{FROST}} - 4$ K. Thus, we conclude that the stratospheric ice clouds as seen by
163 CALIOP were generated due to mountain-wave induced temperature anomalies.

164 *Mountain-wave induced cooling*

165 As documented in Table 1, the magnitude of stratospheric temperature fluctuations ΔT^{SP}
166 measured in the layer from 20 to 25 km increased from values of around 5 K on 26 December
167 2015 to values up to 12 K on 29 and 30 December 2015. These fluctuations are represented by
168 the wave-like temperature perturbations as shown in Fig. 1b. There, the areas of increased
169 backscatter nearly coincide with localized regions of $T < T_{\text{FROST}}$. It must be noted that the
170 CALIPSO satellite trace was nearly aligned with the stratospheric winds as indicated by the
171 orientation of the contour lines of the geopotential height in Fig. 7. Therefore, the ice PSCs as
172 well as the simulated mountain waves are tilted into the ambient stratospheric wind which is
173 oriented from west to east in Fig. 1. The tilting into the ambient wind is characteristic for upward
174 propagating mountain waves (Nappo, 2002).

175 Figure 7 depicts horizontal cross-sections of the stratospheric wave structure at 10 hPa and
176 30 hPa by means of the vertical velocity and the absolute temperature from IFS analyses. A

177 sequence of northwest-southeast oriented updraft-downdraft couplets extends from Svalbard
178 towards the northeast. Altogether, there are four stratospheric cold anomalies associated with the
179 adiabatic cooling in the mountain waves at 10 hPa (Fig. 7 a, c). Their positions clearly correspond
180 to the areas of $T < 185$ K and the CALIOP PSC observations as presented in Fig. 1b. At the lower
181 level of 30 hPa (Fig. 7 b, d), similarly oriented structures exist whereby the cold areas are slightly
182 shifted to the northeast in accordance with the tilt of the observed PSCs (Fig. 1).

183 *Gravity Wave Characteristics*

184 Mountain waves are generated and propagate into the stratosphere if there is a major flow
185 across the topography (low-level forcing), the tropospheric and stratospheric winds are large
186 enough to avoid the formation of wave-induced critical levels, and there is no significant turning
187 of the wind with altitude. All these requirements were satisfied in the Svalbard region for the
188 period from 28 to 30 December 2015. The horizontal wind in the lower troposphere (averaged
189 from 2 to 5 km altitude) increased gradually from about 5 m s^{-1} to about 30 m s^{-1} in the period
190 from 25 to 31 December 2015 as shown by the radiosonde data (Figure 8a). Also near the
191 tropopause level, the averaged wind in the UTLS increased markedly after 28 December up to
192 values of 60 m/s and turned from westerly to southwesterly as the ridge propagated over Svalbard
193 (Table 1). Altogether, the directional shear between tropospheric and stratospheric winds
194 weakened in this period (Fig. 6c). The combination of strong winds in the lower troposphere
195 followed by increased mid- to upper tropospheric winds and the presence of wind of about 25 m
196 s^{-1} in altitudes above (15 to 25 km) created a favorable flow situation for mountain wave
197 excitation and vertical propagation to higher altitudes. Indeed, both the temperature and wind
198 profiles reveal wavelike structures in the stratosphere (Fig. 6) which were analyzed to extract the

199 kinetic and potential energies of the gravity waves as well as their intrinsic frequency and
200 horizontal wavelength from the radiosonde soundings.

201 For this purpose, a polynomial fit is applied to calculate background profiles of the
202 horizontal wind components and the potential temperature from the radiosonde profiles between
203 15 and 25 km altitude. The perturbations calculated as difference between the background
204 profiles and the actual radiosonde profiles are treated as signatures of internal gravity waves from
205 which the kinetic and potential energies are determined according to Murphy et al. (2014). Figure
206 8b shows a peak in the stratospheric kinetic and potential energy densities at 30 December 2015.
207 This enhancement as well as the localized wave appearance over and in the lee of Svalbard (Fig.
208 7) indicate that the waves are generated by the flow above the mountains. Stokes analysis of the
209 velocity perturbations (Eckermann and Vincent, 1989) of the 30 December radio sounding
210 revealed the intrinsic frequency Ω of the dominant gravity wave mode being $6.7f$, where f is the
211 Coriolis parameter. Assuming that the dominant gravity wave mode is a stationary mountain
212 wave its horizontal wavelength can be calculated using the relationship between Ω , horizontal
213 wavenumber k and the background wind U for stationary waves, i.e. $\Omega = -kU$ (Nappo, 2002).
214 Having a background wind of 25 to 35 m s^{-1} (Fig. 8a) the determined horizontal wavelength is
215 approximately 180 ... 250 km. The effect of the Coriolis force alters the dispersion relationship
216 of non-rotating hydrostatic gravity waves and allows a slantwise, e.g. horizontal and vertical,
217 propagation (Gill 1980, Chapter 8). This explains the multiple mountain-wave induced
218 temperature anomalies separated by about 180 km (Fig. 1b and Fig. 7d). Another example of a
219 similar stratospheric cloud structure above Scandinavia and a more detailed discussion can be
220 found in Dörnbrack et al. (2002).

221 The effect of mesoscale temperature fluctuations on the polar cap minimum temperatures T_{MIN} at
222 50 hPa is illustrated by the new IFS cycle 41r2. Figure 2 contains two T_{MIN} curves for a period of
223 3 months when the new IFS cycle was not yet operational. The red line depicts the former IFS
224 cycle 41r1 with 16 km horizontal resolution and the shorter black line is T_{MIN} of the new, updated
225 operational cycle 41r2 with 8 km horizontal resolution. After 8 March 2016, IFS cycle 41r2
226 became operational and continues as red line, Obviously, the higher resolution IFS run achieved
227 much lower T_{MIN} in certain periods, especially at end of December 2015 and at the end of
228 January 2016 when deviations of up to 7 K occurred. These mesoscale temperature fluctuations
229 were generated by mountain wave activities at various places in the Arctic.

230

231 **4. Conclusions**

232 The uniqueness of this contribution to the “picture of the month” is not only justified by the
233 unusual meteorological situation in the Arctic in mid-winter, but also by the co-existence of
234 tropospheric clouds, i.e. cirrus clouds attached to a 12 km high and sharp tropopause, and
235 different types of PSCs between 18 km and 28 km altitude over a limited area poleward of 80°N.
236 Synoptic-scale lifting was responsible for formation of the ice clouds near the tropopause and
237 NAT or STS PSCs in the stratosphere. The total large-scale ascent was also associated with the
238 formation of an ozone mini-hole observed by OMI² which was generally aligned with the
239 tropospheric ridge as shown in Fig. 3, see e.g. Peters et al. (1995) for dynamical aspects of ozone
240 mini-hole formation. Adiabatic cooling in the ascending branches of mesoscale mountain waves
241 dropped the stratospheric temperatures far below the threshold temperature for the existence of
242 ice PSCs. The simultaneous formation of synoptic and mesoscale PSCs inside the Arctic
243 stratospheric vortex happened during a rare meteorological situation during the Northern

² http://ozonewatch.gsfc.nasa.gov/Scripts/big_image.php?date=2015-12-31&hem=N

244 Hemisphere mid-winter. Moreover, it is the remarkable agreement of the simulated wave
245 structure in the IFS short-term forecast and the space-borne observations which indicates a
246 significant trend that the finer resolution and increasing realism of operational NWP model
247 outputs offers a valuable quantitative source for mesoscale flow components which were hitherto
248 not accessible globally.

249

250 **Appendix**

251 *Numerical weather prediction model data*

252 Operational analyses of the integrated forecast system (IFS) of the European Centre of Medium
253 Range Weather Forecasts (ECMWF) are used to provide meteorological data to characterize the
254 atmospheric situation. The operational analyses and forecasts of the deterministic high-resolution
255 (HRES) IFS cycle 41r2 have a horizontal resolution of about 8 km (T_C1279) and 137 vertical
256 levels ($L137$)³. The model top is located at 0.01 hPa. The enhanced horizontal resolution was
257 achieved by changing from linear (T_L) to cubic (T_C) spectral truncation and introducing an
258 octahedral reduced Gaussian grid. With the cubic spectral truncation the shortest resolved wave is
259 represented by four rather than two grid points and the octahedral grid is globally more uniform
260 than the previously used reduced Gaussian grid (Malardel and Wedi, 2016). In December 2015,
261 the IFS cycle 41r2 was not yet in its operational mode but products were disseminated among the
262 users. So, we were able to retrieve forecasts and analysis fields for the current contribution.

263 *CALIPSO data*

³ <https://software.ecmwf.int/wiki/display/FCST/Implementation+of+IFS+cycle+41r2> and
<http://www.ecmwf.int/en/about/media-centre/news/2016/new-forecast-model-cycle-brings-highest-ever-resolution>

264 The primary instrument on CALIPSO is a lidar (CALIOP, or Cloud-Aerosol Lidar with
265 Orthogonal Polarization) that measures backscatter at wavelengths of 1064 nm and 532 nm, with
266 the 532-nm signal separated into orthogonal polarization components parallel and perpendicular
267 to the polarization plane of the outgoing laser beam. A description of CALIOP and its on-orbit
268 performance can be found in Hunt et al. (2009), and details on calibration of the CALIOP data
269 are provided by Powell et al. (2009). CALIOP has proven to be an excellent system for observing
270 PSCs (Pitts et al., 2007; 2009; 2011; 2013).

271

272 **Acknowledgements**

273 Part of this research was funded by the German research initiative “Role of the Middle
274 Atmosphere in Climate (ROMIC)” funded by the German Ministry of Research and Education in
275 the project “Investigation of the life cycle of gravity waves (GW-LCYCLE)”. Access to the
276 ECMWF data was possible through the special project “HALO Mission Support System”. The
277 presented radiosonde data were obtained at the AWIPEV research base at Ny-Ålesund, Svalbard.
278 They are part of the Global Climate Observing Systems (GCOS) Reference Upper-Air Network
279 (GRUAN), available via the webpage www.gruan.org.

280 **References**

281 Backhouse, W., 1885: Iridescent clouds, *Nature*, **31**, 192–193.

282
283 Browell, E. V. , C. F. Butler, S. Ismail, P. A. Robinette, A. F. Carter, N. S. Higdon, O. B. Toon,
284 M. R. Schoeberl, and A. F. Tuck, 1990: Airborne lidar observations in the wintertime Arctic
285 stratosphere: polar stratospheric clouds, *Geophys. Res. Lett.*, **17**, 385–388.

286
287 Carslaw, K. S., and Coauthors, 1998: Increased stratospheric ozone depletion due to mountain-
288 induced atmospheric waves. *Nature*, **391**, 675–678.

289
290 Dee, D., and Coauthors, 2011: The ERA-Interim reanalysis: Configuration and performance of
291 the data assimilation system. *Quart. J. Roy. Meteor. Soc.*, **137**, 553–597.

292
293 Dörnbrack, A., M. Leutbecher, H. Volkert, and M. Wirth, 1998: Mesoscale forecasts of
294 stratospheric mountain waves. *Meteor. Appl.*, **5**, 117–126.

295
296 Dörnbrack, A., T. Birner, A. Fix, H. Flentje, A. Meister, H. Schmid, E. V. Browell, and M. J.
297 Mahoney, 2002: Evidence for inertia gravity waves forming polar stratospheric clouds over
298 Scandinavia. *J. Geophys. Res.* 107(D20), 8287, doi:10.1029/2001 JD000452

299
300 Dye, J. E., D. Baumgardner, B. W. Gandrud, K. Drdla, K. S. Barr, D. W. Fahey, L. A. DelNegro,
301 A. Tabazadeh, H. H. Jonsson, J. C. Wilson, M. Loewenstein, J. R. Pdolske, and K. R. Chan,
302 1996: In-situ observations of an Antarctic polar stratospheric cloud: Similarities with Arctic
303 observations. *Geophysical Research Letters*, 23, 1913-1916, DOI: 10.1029/96GL01812.

304 Eckermann, S. D. and R. A. Vincent, 1989: Falling sphere observations of anisotropic gravity
305 wave motions in the upper stratosphere over Australia. *Pure Appl. Geophys.*, **130**, 509–532.

306
307 Eckermann, S. D., A. Dörnbrack, H. Flentje, S. B. Vosper, M. J. Mahoney, T. P. Bui, and K. S.
308 Carslaw, 2006: Mountain Wave–Induced Polar Stratospheric Cloud Forecasts for Aircraft
309 Science Flights during SOLVE/THESEO 2000. *Wea. Forecasting*, **21**, 42–68. doi:
310 [10.1175/WAF901.1](https://doi.org/10.1175/WAF901.1)

311
312 Geelmuyden, H, 1885: Iridescent clouds, *Nature* **31**, 264.

313
314 Gill, A. E., 1982: *Atmosphere-Ocean Dynamics*, Academic Press, 662 pp

315
316 Hólm, E., R. Forbes, S. Lang, L. Magnusson, and S. Malardel, 2016: New model cycle brings
317 higher resolution, ECMWF Newsletter, Spring 2016, 14-19.
318 <http://www.ecmwf.int/sites/default/files/elibrary/2016/16299-newsletter-no147-spring-2016.pdf>

319
320
321 Hu, J., R. Ren, and H. Xu, 2014: Occurrence of winter stratospheric sudden warming events and
322 the seasonal timing of spring stratospheric final warming, *J. Atmos. Sci.*, **71**, 2319–2334, doi:
323 10.1175/JAS-D-13-0349.1.

324
325 Di Liberto, L., F. Cairo, F. Fierli, G. Di Donfrancesco, M. Viterbini, T. Deshler, and M. Snels,
326 2014: Observation of Polar Stratospheric Clouds Over McMurdo (77.85°S, 166.67°E) (2006-
327 2010). *J. Geophys. Res.*, **119**, 5528–5541.

328

329 Liu, Z., Vaughan, M. A., Winker, D. M., Hostetler, C. A., Poole, L. R., Hlavka, D., Hart, W., and
330 McGill, M., 2004: Use of probability distribution functions for discriminating between cloud and
331 aerosol in lidar backscatter data, *J. Geophys. Res.*, **109**, D15202, doi:10.1029/2004JD004732.

332

333 Malardel, S. and N. P. Wedi, 2016: How does subgrid-scale parametrization influence nonlinear
334 spectral energy fluxes in global NWP models?, *J. Geophys. Res.*, **121**,
335 doi:10.1002/2015JD023970.

336

337 Manney, G. L. and Z. D. Lawrence, 2016: The major stratospheric final warming in 2016:
338 Dispersal of vortex air and termination of Arctic chemical ozone loss, *Atmos. Chem. Phys.*
339 *Discuss.*, doi:10.5194/acp-2016-633, in review.

340

341 Maturilli, M. and A. Dörnbrack, 2006: Polar stratospheric ice cloud above Spitsbergen, *J.*
342 *Geophys. Res.* **111**, D18, D18210, doi:10.1029/2005JD006967.

343

344 Mohn, H., 1893, Irisirende Wolken, *Meteorol. Z.* **11**, 81–97.

345

346 Murphy, D. J., Alexander, S. P., Klekociuk, A. R., Love, P. T., and Vincent, R. A., 2014:
347 Radiosonde observations of gravity waves in the lower stratosphere over Davis, Antarctica, *J.*
348 *Geophys. Res.*, **119**, 11973–11996, doi:10.1002/2014JD022448.

349

350 Nappo, C. J., 2012: *An Introduction to Atmospheric Gravity Waves*, 2nd Edition, Academic Press,
351 400 pp.

352

353 Peter, T. 1997: Microphysics and heterogeneous chemistry of polar stratospheric clouds. *Annu.*
354 *Rev. Phys. Chem.* **48**, 785–822.

355

356 Peters, D., J. Egger, and G. Entzian, 1995: Dynamical aspects of ozone mini-hole formation.
357 *Meteor. Atmos. Phys.*, **55**, 205–214.

358

359 Pitts, M. C., Thomason, L. W., Poole, L. R., and Winker, D. M, 2007: Characterization of polar
360 stratospheric clouds with spaceborne lidar: CALIPSO and the 2006 Antarctic season, *Atmos.*
361 *Chem. Phys.*, **7**, 5207–5228.

362

363 Pitts, M. C., Poole, L. R., Thomason, L. W.: CALIPSO polar stratospheric cloud observations:
364 second-generation detection algorithm and composition discrimination, *Atmos. Chem. Phys.*, **9**,
365 7577-7589, 2009.

366

367 Pitts, M. C., Poole, L. R., Dörnbrack, A., and Thomason, L. W., 2011: The 2009-2010 Arctic
368 Polar Stratospheric Cloud Season: A CALIPSO Perspective, *Atmos. Chem. Phys.*, **11**, 2161–
369 2177.

370

371 Reichardt, J., A. Dörnbrack, S. Reichardt, P. Yang, and T. J. McGee, 2004: Mountain wave PSC
372 dynamics and microphysics from ground-based lidar measurements and meteorological
373 modeling, *Atmos. Chem. Phys.*, **4**, 1149–1165

374

375 Reichardt, J., S. Reichardt, C. Hostetler, P. Lucker, T. McGee, L. Twigg, A. Dörnbrack, M.
376 Schoeberl, and P. Yang, 2015: Mother-of-pearl cloud particle size and composition from aircraft-
377 based photography of coloration and lidar measurements, *Appl. Opt.*, **54**, B140–B153.
378

379 Rosen, J. M., N. T. Kjöme, V. U. Khattatov, V. V. Rudakov, and V. A. Yushkov, 1992:
380 Observations of ozone and polar stratospheric clouds at Heiss Island during winter 1988–1989, *J.*
381 *Geophys. Res.*, **97**, 8099–8104, doi:[10.1029/91JD02524](https://doi.org/10.1029/91JD02524).
382

383 Solomon, S., 1999: Stratospheric ozone depletion: a review of concepts and history. *Rev.*
384 *Geophys.* **37**, 275–316.
385

386 Stanford, J. L. and Davies, J. S. 1974: A century of stratospheric cloud reports: 1870–1972. *Bull.*
387 *Am. Meteorol. Soc.* **55**, 213–219.
388

389 Störmer, C. 1929: Remarkable clouds at high altitudes. *Nature*, **123**, 940–941.
390

391 Störmer, C. 1931: Höhe und Farbverteilung der Perlmutterwolken. *Geofysiske Publikasjoner* **IX**,
392 3–25.
393

394 Strawa, A. W., K. Drdla, M. Fromm, R. F. Pueschel, K. W. Hoppel, E. V. Browell, P. Hamill,
395 and D. P. Dempsey, 2002: Discriminating Types Ia and Ib polar stratospheric clouds in POAM
396 satellite data, *J. Geophys. Res.*, **107**, 8291, doi:10.1029/2001JD000458.
397

398 Teitelbaum, H. and R. Sadourny, 1998: The role of planetary waves in the formation of polar
399 stratospheric clouds, *Tellus A*, **50**, 302–312.

400 **Tables**

401

Date	T^{TP} / K	$V_{\text{H}}^{\text{TP}} / \text{m s}^{-1}$	$\alpha^{\text{TP}} / \text{K}$	T^{SP} / K	$\Delta T^{\text{SP}} / \text{K}$
26 Dec 2015	209.3	8.7	254	188.8	4.7
27 Dec 2015	209.6	27.7	296	187.4	6.5
28 Dec 2015	205.9	23.3	268	187.3	8.4
29 Dec 2015	200.0	23.6	240	184.4	12.0
30 Dec 2015	204.7	36.8	241	185.4	10.1
31 Dec 2015	204.1	59.8	199	183.9	6.8

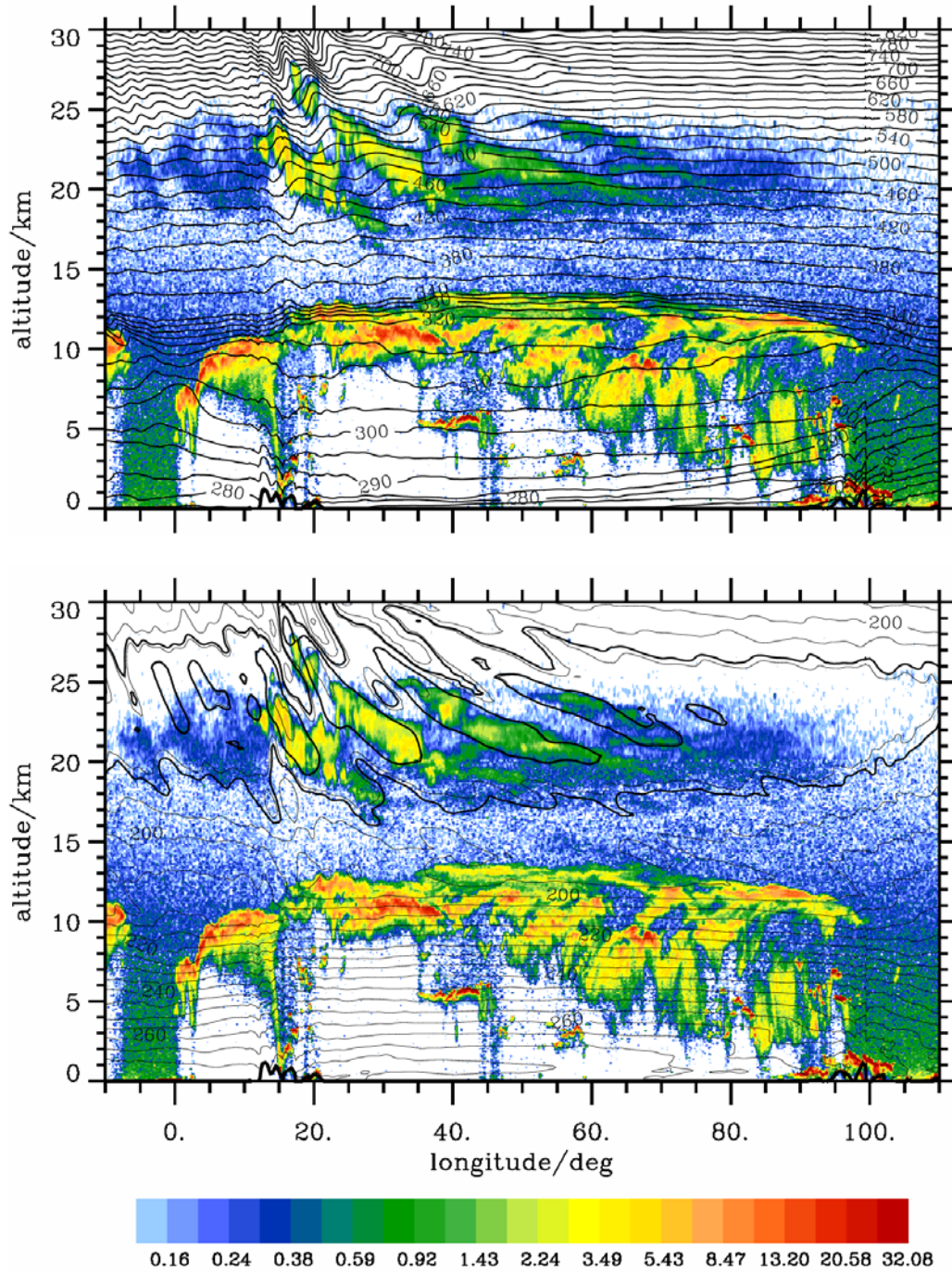
402

403 **Table 1:** Mean quantities in the UTLS averaged from 10 to 13 km altitude: absolute temperature
404 T^{TP} , horizontal wind V_{H}^{TP} , and wind direction α^{TP} from the radiosonde soundings in Ny-Ålesund.
405 The mean stratospheric temperature T^{SP} is averaged from 20 to 25 km altitude and ΔT^{SP} is the
406 difference between the measured maximum and minimum T in this layer.

407 **Figures**

408

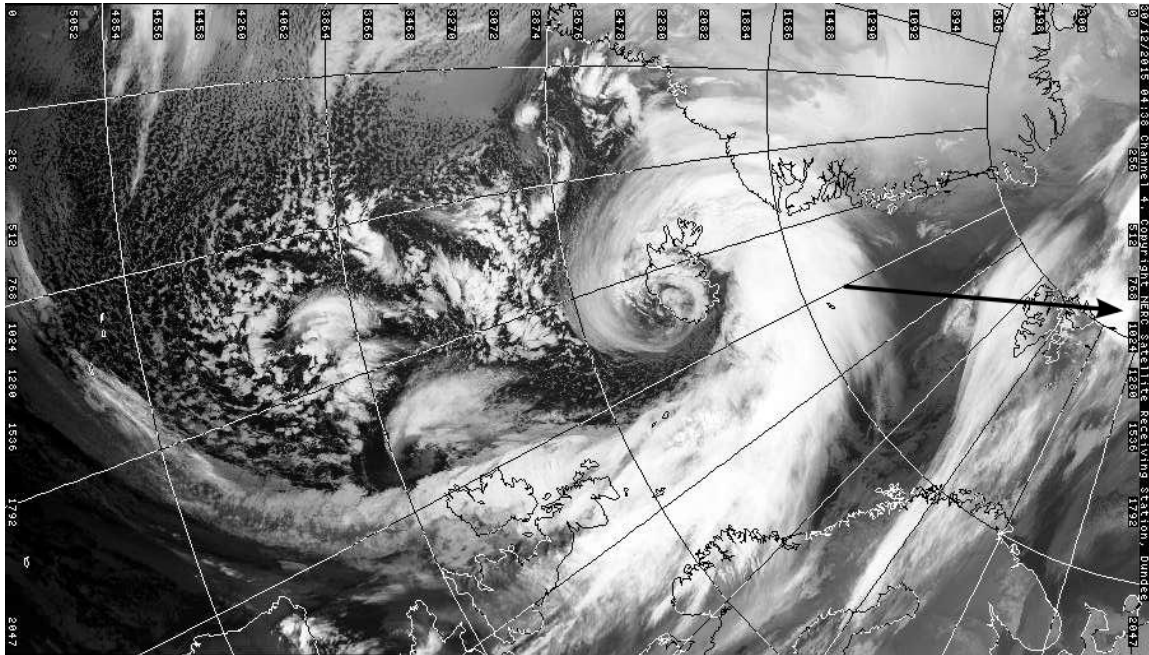
409



410

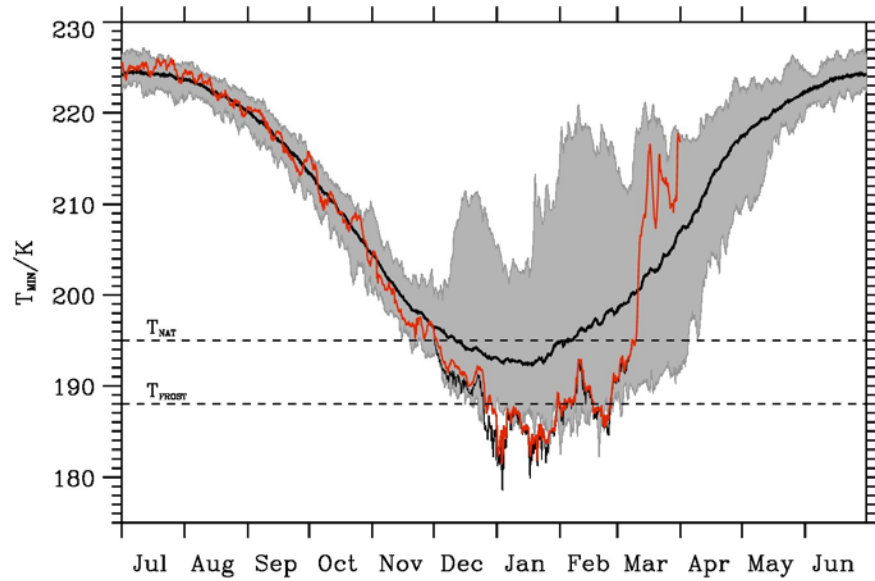
411

412 **Figure 1:** Composite of 532 nm total attenuated backscatter ($10^{-3} \text{ km}^{-1} \text{ sr}^{-1}$, color shaded) from CALIOP
413 and ECMWF potential temperature (top, K, solid black lines) and absolute temperature (bottom, K, thin
414 black lines every 5 K and thick black lines at 185 K and 191 K) valid on 30 December 2015 at 04 UTC (+
415 4 h lead time from the 00 UTC high res IFS forecast of cycle 41r2.



416 **Figure 2:** Thermal infra-red image (NOAA 19, channel 4: 10.3-11.3 μ m) on 30 December 2015 0440 UTC
417 with the first third of the path of the CALIOP measurements (Fig. 1) as black arrow. Image provided by
418 NERC Satellite Receiving Station, Dundee University, Scotland (<http://www.sat.dundee.ac.uk>).

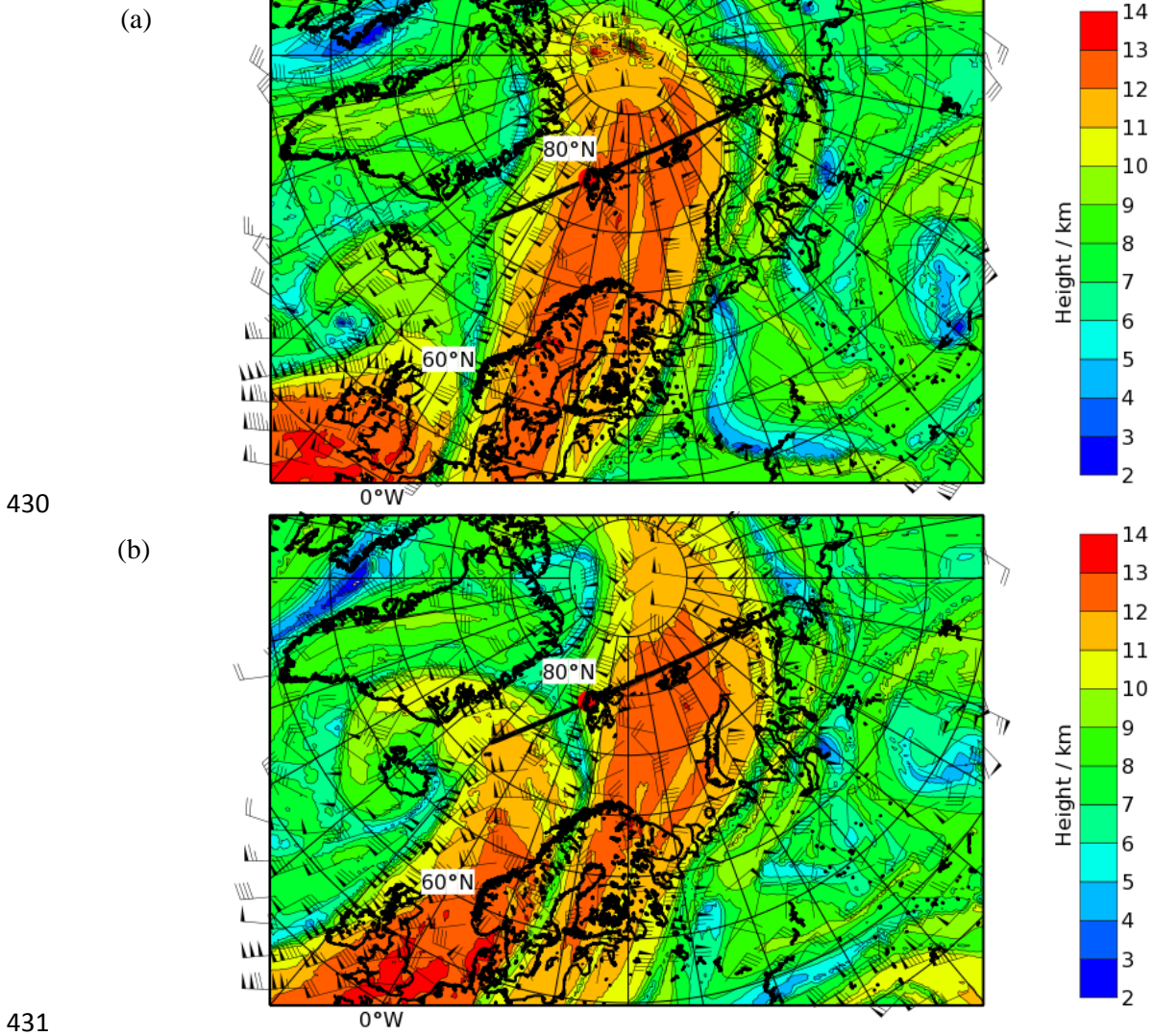
419



420

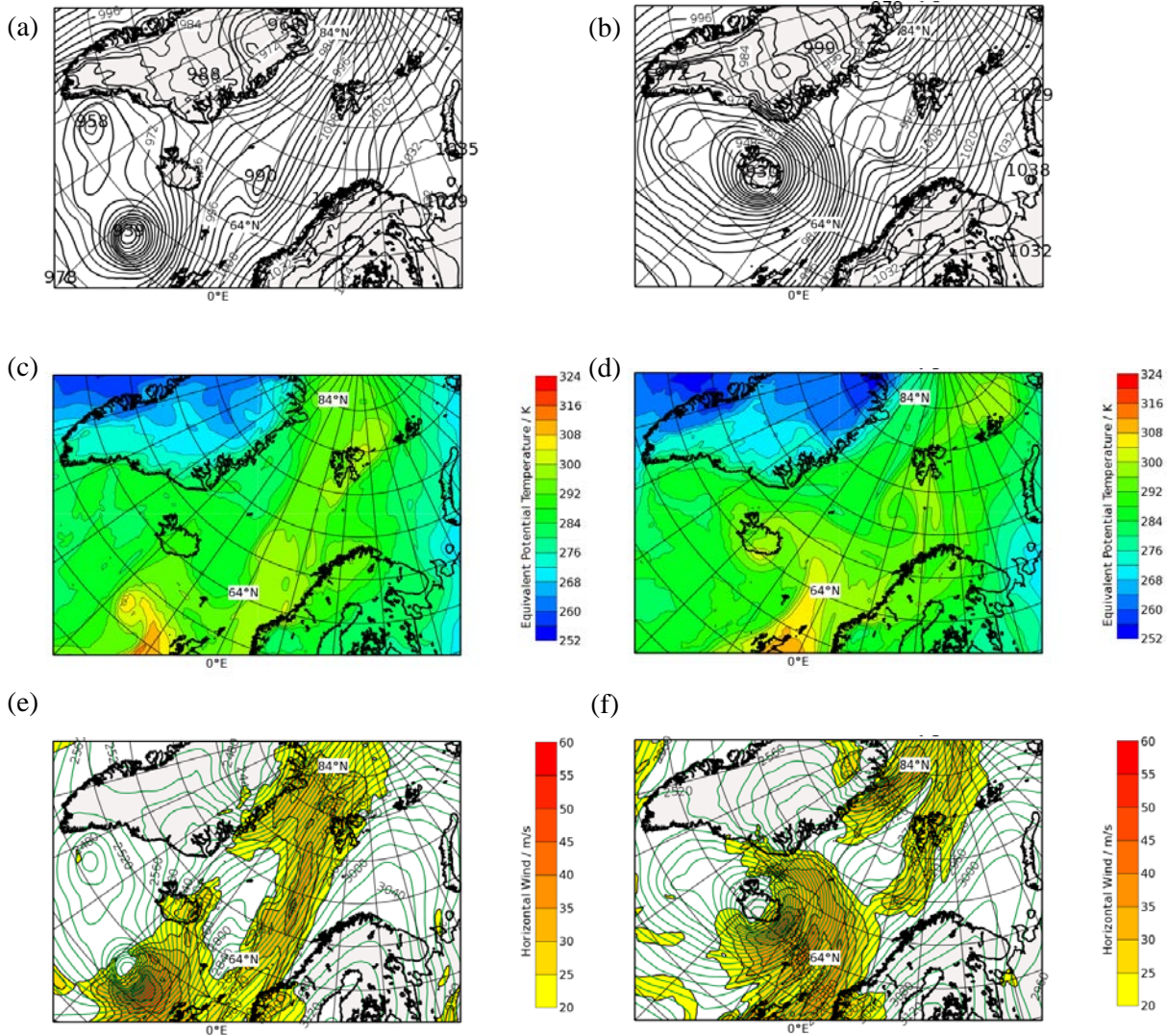
421 **Figure 3:** 6 hourly ECMWF reanalyses interim (ERA-Interim, Dee et al., 2011) data retrieved at a
 422 horizontal resolution of 1° : Minimum temperature T_{MIN} (K) between 65°N to 90°N at the 50 hPa pressure
 423 surface. Thick black line denotes the mean values of T_{MIN} averaged from 1979 – 2015, the shaded areas
 424 encompass the minimum and maximum values of T_{MIN} attained at every date between 1979 and 2015.
 425 The red line marks the evolution of T_{MIN} from operational analyses of the IFS cycle 41r1 until 8 March
 426 2016. The thin black line indicates T_{MIN} from the IFS cycle 41r2 in the pre-operational phase 1 December
 427 2015 until 8 March 2016 retrieved at a resolution of 0.125° . After 8 March 2016, the black line continues
 428 as red curve of the operational IFS cycle 41r2.

429



432 **Figure 4:** Height of the dynamical tropopause (km, color shaded) and horizontal wind (m s^{-1} , barbs) at the
 433 2 PVU surface on 29 December 2015 18 UTC (a) and 30 December 2015 06 UTC (b). The path of the
 434 CALIPSO overpass is plotted as solid black line, the location of Ny-Ålesund, Svalbard is marked by a red
 435 dot.

436



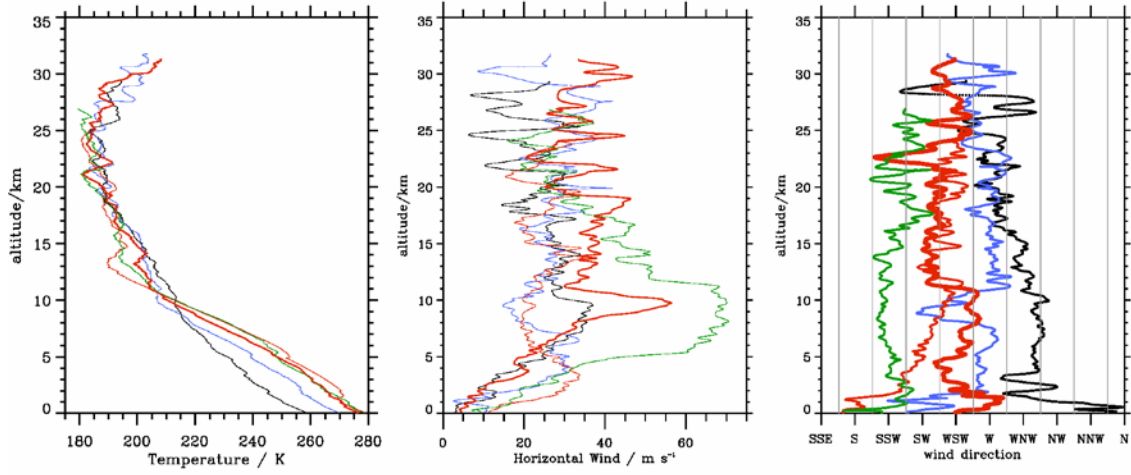
437

438

439

440 **Figure 5:** Tropospheric charts valid on 29 December 2015 18 UTC (left column) and 30 December 2015
 441 06 UTC (right column). (a,b): Mean sea level pressure (hPa, contour lines), (c,d): Equivalent potential
 442 temperature (K, color shaded) at 850 hPa, and (e,f): horizontal wind (m s^{-1} , color shaded) and geopotential
 443 height (m, contour lines) at 700 hPa.

444



445

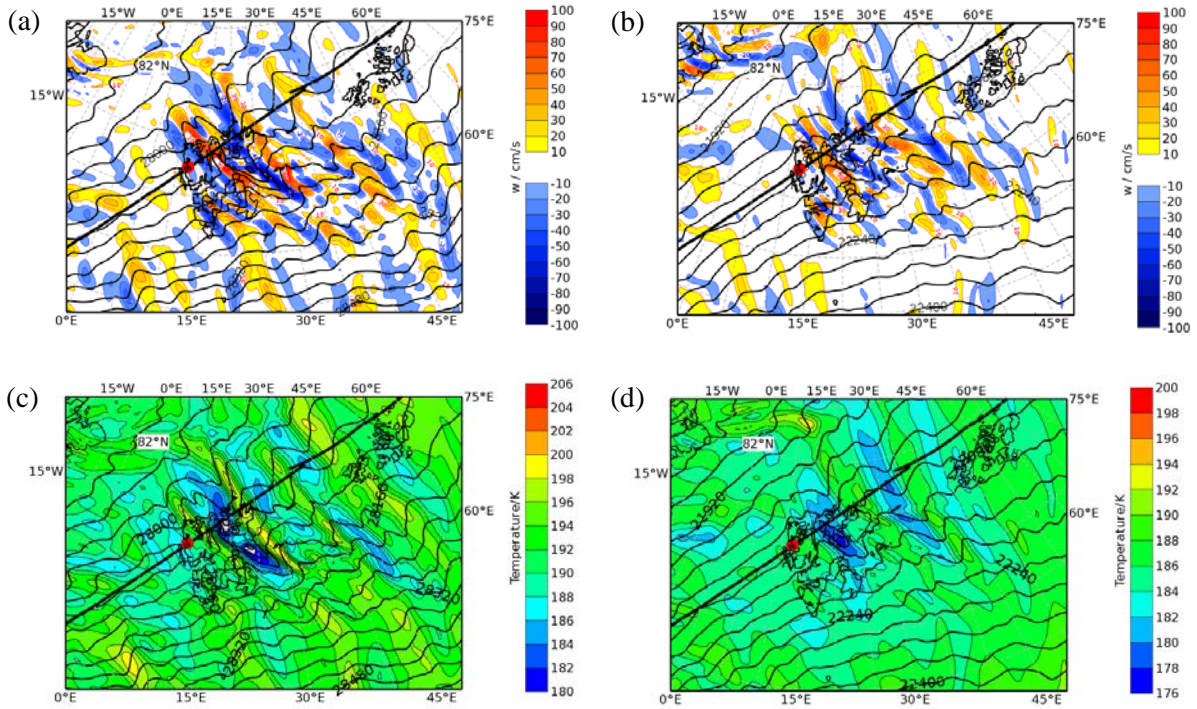
446 **Figure 6:** Vertical profiles of absolute temperature (a), horizontal wind (b), and wind direction (c) from
447 radiosonde launches in Ny-Ålesund, Svalbard on 27 December (black), 28 December (blue), 29 December
448 (thin red), 30 December (thick red), and 31 December (green) 2015 12 UTC, respectively.

449

450

451

452

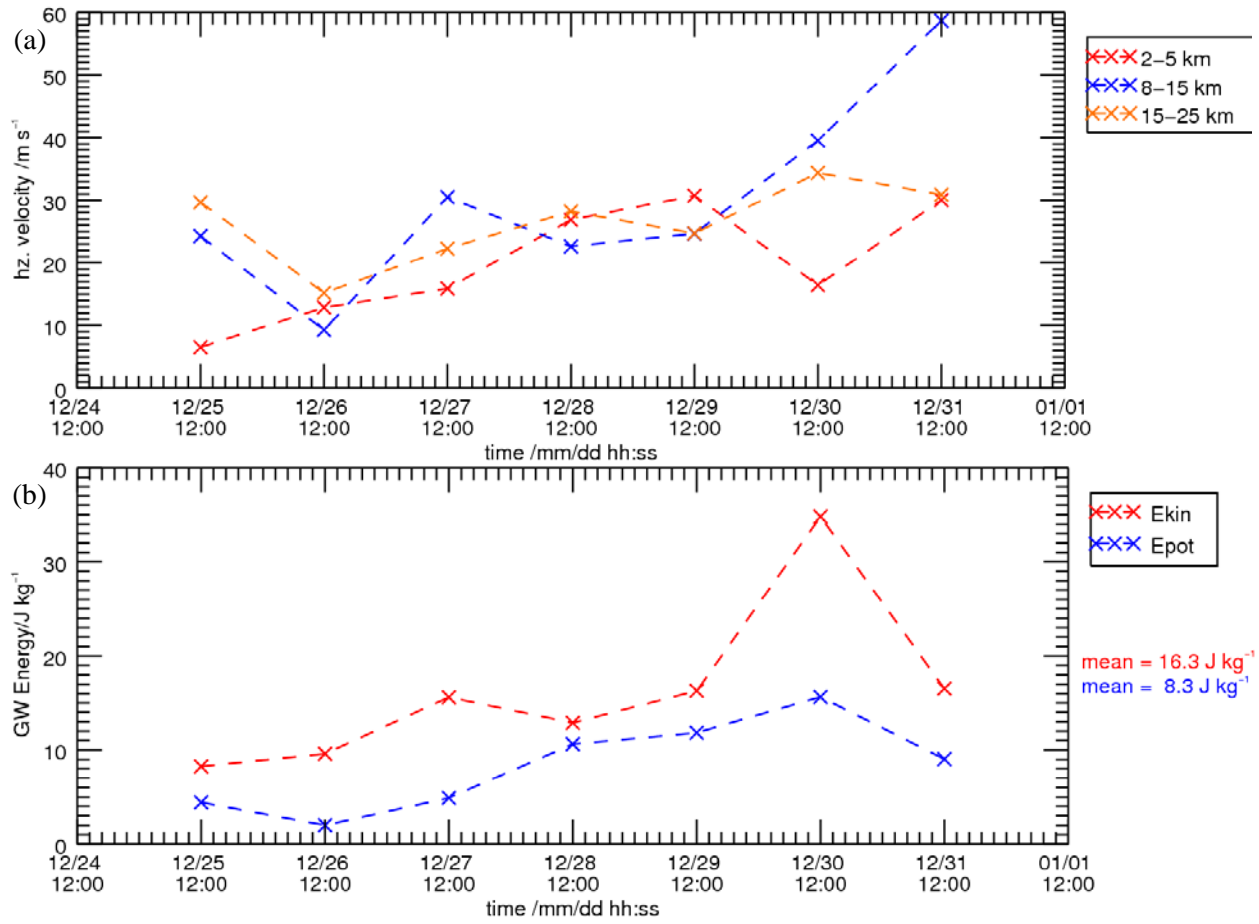


453

454

455

456 **Figure 7:** Vertical velocity (m s^{-1} , color shading, top row), absolute temperature (K, color shading, bottom
457 row), and geopotential height (m, black contour lines) from the IFS cycle 41r2 at 10 hPa (a, c) and at 30
458 hPa (b,d) valid on 30 December 2015 06 UTC. The path of the CALIPSO overpass is plotted as solid
459 black line, the location of Ny-Ålesund, Svalbard is marked by a red dot.



460

461

462

463

464

465

466

Figure 8: (a) Vertically averaged horizontal wind in the lower troposphere (2 to 5 km, red crosses), the tropopause region (8 to 15 km, blue crosses), and in the stratosphere (15 to 25 km, yellow crosses). (b) Stratospheric gravity wave kinetic and potential energies (red and blue crosses, respectively) determined from the radiosonde soundings of Ny-Ålesund, Svalbard in an altitude range of 15 to 25 km.